SI Appendix

Force generation by groups of migrating bacteria

Benedikt Sabass[a,b], **Matthias D. Koch**[c], **Guannan Liu**[c,d], **Howard A. Stone**[a], **and Joshua W. Shaevitz**[c,d]

[a]Department of Mechanical and Aerospace Engineering, Princeton University, NJ 08544, USA; [b]Institute of Complex Systems 2, Forschungszentrum Jülich, Jülich, Germany; [c]Lewis-Sigler Institute for Integrative Genomics, Princeton University; [d]Joseph Henry Laboratories of Physics, Princeton University

List of Figures

1. Cell culture

M. xanthus strains employed in this study are a wild-type DZ2 strain, the gliding-deficient strain TM 146 DZ2 $\Delta aglQ$ (1), and a pilus-deficient strain DZ2 AglZ-YFP $\Delta pilA$. The double mutant $\Delta pilA$, $\Delta aglQ$ (2, 3) and a mutant with deficient pilus retraction machinery $\Delta pilT$ (EM589) were used as control. *M. xanthus* bacteria are grown overnight at 32° C in CYE medium at pH 7.8 consisting of 1 % (w/v) Casitone, 0.5 % yeast extract, 10 mM 3-(N-morpholino) propanesulfonic acid (MOPS), and 4 mM MgSO$_4$. To remove nutrients from the medium prior to experiments, cells are washed once in TPM (10 mM Tris-HCl, pH 7.6, 1 mM KH$_2$PO$_4$, 8 mM MgSO$_4$). The suspension of bacteria in TPM is briefly vortexed to ensure homogeneity before depositing it on the gel for imaging.

2. Preparation and characterization of elastic substrates for TFM

Polyacrylamide gels were prepared as described in (4) for use with fluorescent beads of two colors. We prepare $250\,\mu$l gel with final concentrations of 3% polyacrylamide and 0.06% bisacrylamide. The gel consists of water, polyacrylamide solution (40 %), bisacrylamide solution (2 %), each $4.5\,\mu$l of orange and dark red fluorescent beads (FluoSpheres, diameter $0.040\,\mu$m, carboxylate-modified, (565/580) nm and (660/680) nm), and $1.5\,\mu$l of freshly prepared ammonium persulfate solution (10 % in water). Polymerization is initiated with $0.75\,\mu$l of N,N,N',N'-tetramethylethylenediamine (TEMED). $40\,\mu$l of the forming gel is spotted on a plasma-treated microscope slide or a glass-bottom petri dish and covered with a hydrophobic cover slip. After waiting for one hour to let the gel polymerize, the top coverslip is carefully removed and the gels are washed with water. If washing of gels is insufficient, bacteria can not survive on the gel, which we attribute to unpolymerized gel constituents.

Elastic properties of the PAA gel are measured by a stress-controlled rheometer (Anton Paar, Physica MCR 301). All of the rheometry measurements are carried out at 23°C with plate diameters of 50 mm. To avoid slippage between the gel and rheometer plates, we employ a parallel-plate geometry with sand-blasted plates of roughness $[8-9]\,\mu$m (PP50/S). The gap thickness is chosen to be 0.5 mm. Using a cone-plate geometry to obtain a homogeneous velocity gradient throughout the sample (Measuring cone CP50-1/TG) yielded similar results. After preparing the gel and adding the polymerization initiator, the liquid is placed on the rheometer and the measurement plate is moved into measurement position. After letting the gel polymerize between the plates for 15 min, the rim of the plates is covered with a small film of water to avoid evaporation. Polymerization is allowed to proceed for $45-60$ min before data recording to ensure that the elastic properties reached stationary values. Gelation of the substrate produces significant normal forces on the rheometer plate, which can affect the measurement of shear moduli. Therefore, the normal forces are set to zero by slight adjustment of the gap size before before commencing the measurement. For the employed PAA gel (3% PAA, 0.06% BIS), we obtain an elastic shear modulus of $G' = 121$ Pa from 11 measured gels with a sample standard deviation of 43Pa (see Ref. (5) for literature values). Assuming a Poisson ratio close to 1/2, the Young modulus is estimated as $E = 2(1 + \nu)G' \simeq 360$ Pa. At typical oscillation frequencies of $[0.01\dots10]$ Hz, the loss modulus is found to be small, $G'' = 6$ Pa with a sample standard deviation of 5 Pa.

Alternative TFM substrates could be made of agarose gels, which, however, have a number of disadvantages. First, the mechanical properties are not as well characterized as for PAA and the rigidity depends on temperature. Second, the elastic moduli of agarose assays are usually on the order of kPa, which is much more rigid than our PAA gels, leading to tiny

deformations that are hardly measurable. Preliminary tests indeed indicated that *M. xanthus* does not deform a 1% agarose gel appreciably. Finally, the pore size of agarose is not small enough to trap nanometer-sized beads, which makes it necessary to chemically crosslink beads with the gel.

3. Coating of substrates with chitosan

Chitosan, a deacetylated form of chitin, is a polysaccharide that has broad biocompatibility. We found that PAA gels coated with chitosan can be used as motility assays where, depending on the concentration of chitosan, myxobacteria can move individually and in groups (6). To coat the gels, we dissolve 10 mg chitosan in 3 ml of 0.2 M acidic acid by gentle pipetting. The solution is then diluted 1/50 with DI-water. After gently removing excess water from the gel surface, 100 μl of the chitosan solution is placed on the gels and left there for at least one hour. Prior to imaging, gels are washed three times with a tris buffer solution. To prepare the sample for imaging, about 7 μl of cell suspension in TPM are spotted on the gel and excess liquid is removed with a tissue. Finally, a cover slip is gently placed on top of the sample.

4. Imaging

Imaging is was on a Nikon Ti-E confocal microscope with Perfect Focus System, where a Yokogawa spinning disc (CSU-21) is mounted with a quad dichroic accommodating lasers with wavelengths of 405, 488, 561, and 647 nm. Images were taken with a Hamamatsu ImageM back thinned EMCCD or an ORCA Flash digital CMOS camera. Individual bacteria were imaged through the glass coverslip above the cells using a 100× oil immersion objective with 1.5 magnification. To avoid applying vertical pressure on bacterial groups that are occasionally thicker than the slit between sample and gel, some samples were imaged from below by using a glass-bottom dish as support for the gel. Focusing through the whole gel then required matching the refractive index by use of a 60× water immersion objective with 1.5 magnification. We observed that imaging with high laser intensity reduces motility of bacteria, which likely results from photodamage. Therefore, the laser light intensity was kept very low while long exposure times up to one second still allowed to obtain high-quality images.

5. Traction reconstruction

To avoid evaporation and allow bacterial migration, it was necessary to cover the sample with a glass slip, where a thin spacer maintained a micron-scale distance between the glass slip and gel. If one wishes to image only the gel without bacteria to obtain a stress-free reference image of the beads, the delicate setup would have to be disassembled under the microscope. This task proved unfeasible. Therefore, a stress-free reference image for tracking of the fluorescent marker beads is not available. Thus, we employed the first frame of a time-lapse series as reference frame. Consequently, the displacements and calculated tractions are those that occur relative to the first frame of a movie. Computational analysis of gel deformation and traction force estimation is done as described previously (4, 7). Briefly, we employ a correlation-based tracking procedure that allows to extract deformation information simultaneously from both image channels. At the position x, y, the displacement field $u_i(x, y)$ is related to a traction field $t_i(x', y')$ through convolution with a Green's function G_{ij} as $u_i(x, y) = \int G_{ij}(x - x', y - y')t_i(x', y') \mathrm{d}x'\mathrm{d}y'$ where the integral extends over the whole gel surface plane (8). We estimate the traction field that produces the measured displacement field by inverting the convolution equation in Fourier space while regularizing the traction magnitude. A constant regularization parameter value was employed for the whole data analysis. Edge-effects resulting from solving the system in Fourier space are avoided by zero-patterning the edges of the displacement field.

6. Estimation of point force magnitude

For inferring the force magnitude at hotspots, we modify established methods (4, 9). As an important improvement, we assume here that the beads are located a finite distance beneath the surface of the gel. We assume Cartesian coordinates x_1, x_2, z, where an elastic material is bounded by the x_1, x_2 plane and occupies the upper half space $z > 0$. The elastic Young modulus is denoted by E and Poisson's ratio is denoted by ν. Forces acting in the x_1, x_2 plane are denoted by $F_{1,2}$. Vertical forces are assumed to be zero. The displacements in a plane parallel to the material surface are denoted by $u_i(x_1, x_2, z)$, where we assume that $z \geq 0$ is a constant. In a linear framework, we first consider a point force applied at the origin. Then, material displacements are related to the force through $u_i(x_1, x_2, z) = \sum_{j=1,2} G_{ij}(x_1, x_2, z)F_j$ with a Green's function

$$G_{ij}(x_1, x_2, z) = \frac{(1+\nu)}{2\pi E} \left[\frac{2(1-\nu)r + z}{r(r+z)}\delta_{ij} + \frac{(2r(\nu\, r + z) + z^2)\, x_i x_j}{r^3(r+z)^2} \right]. \qquad [1]$$

The measured displacements can be treated as resulting from the superposition of point forces at various locations. Thus, we can write a linear system relating displacements with index n to point forces with index m as $u_{i,n} = \tilde{G}_{i,j,n,m}F_{j,m}$. We employ an established procedure to solve the inverse problem by using a singular value decomposition of $\tilde{G}_{ij,nm}$ and Tikhonov regularization where the expression $\sum_{i,j,n,m} |u_{i,n} - \tilde{G}_{ij,nm}F_{j,m}|^2 + \lambda^2|F_{j,m}|^2$ is minimized. Here, λ is a regularization parameter. Figures S12A,B,C illustrate the process of force estimation. First, we employ the results from standard traction force microscopy

to localize hotspots of traction. Then, we manually place a point force into the center of every hotspot. Using the such defined point force locations together with the measured substrate displacements, we calculate the forces F_i. In Fig. S12D we plot the originally measured displacements together with the displacements resulting from the calculated forces. Differences between measurements and calculation illustrate the approximative nature of the technique. In Fig. S12E we compare the results from four independent experiments. Average values of forces differ slightly, but are on the order of $100\,\mathrm{pN}$. In Fig. S12E we investigate the influence of the vertical distance z between imaging plane and gel surface. Side-view of a vertical scan through the sample illustrates our choice for the imaging plane. As a result of the finite point spread function and the difficulty to determine the exact location of the gel surface, the value of z is uncertain. However, we determined z to lie in the range of $[0.2-1]\,\mu\mathrm{m}$ and therefore assume a constant value of $z = 0.5\,\mu\mathrm{m}$ for all experiments. From Fig. S12E, it can be seen that the force magnitude varies depending on the choice of z. Therefore, incorporating the position of the focal plane into the calculation results in a significantly improved force estimate. Fig. S12F shows our choice of the regularization parameter. The magnitude of forces decreases rather sharply at $\lambda \sim 1$. To maintain consistency among the samples, we employ for all experiments $\lambda = 0.01$. This value is for all samples below the transition to the regularization-dominated regime where force magnitude is strongly suppressed.

7. Effect of prestress on the traction error

The substrate deformations are measured against a reference that is usually the first frame of an image sequence. Traction analysis is commenced a few minutes after the first image. Measuring deformations relative to a reference that contains cells can yield a deformation field that is a superposition of the deformations produced in the present frame minus the deformations in the reference frame (Fig. S13D-G). Since TFM is based on the assumption of linear elasticity, reconstructed tractions are also a superposition of the traction in the current frame with the prestress in the reference frame. If the areas with traction in reference frame and current frame do not overlap, prestress is rather unproblematic. However, prestress may cause an increase or decrease of the measured values if the regions of traction and prestress are not spatially separated.

In Fig. S13D (I-III) we show simulation studies to illustrate the potential strong effect of prestress in a single frame. Traction magnitudes are affected by prestress and lead to an error around $\sim 20\%$ in the traction median (Fig. S13G). Prestress also increases the width of the distribution of measured traction values. Fig. S13G shows multiple simulation results using variable locations of the traction spots. In spite of the errors caused by prestress, samples with different traction magnitudes can be clearly distinguished. Fig. S13G shows traction values with and without prestress in three simulations with different applied traction. Clearly, the relative traction magnitude with prestress is similiar to the relative traction magnitudes without prestress. To reduce this error even more, we consider data from at least 10 frames per experiment and multiple experiments. Note that other factors also cause considerable errors in the continous traction field. Most notably, the spatial undersampling of the displacement field leads to an underestimation of traction magnitude. Thus, traction magnitude estimates as in Fig. 4F should not be understood as precise absolute measurements, but rather as estimates of the relative strength of mechanical activity.

For analysis of the experimental data on point force magnitudes in hotpots (Figs. 2B,3F), we simply consider all hotspots, including those that could result from cells that only were present in the reference frame. To compensate for errors that result from potentially overlapping hotspots we consider at least 5 frames for each experiment and multiple experiments. Note that estimating forces using the assumption of point forces also produces considerable statistical errors (4).

For studying the position of hotspots relative to migrating individual cells (Fig. 2B), we excluded traction that was stationary and thus likely to result from background.

8. Data presentation and correlation measures

The histograms in figures were prepared by choosing a bin width w that is close to the value given by the heuristic rule $w = 3.49\,\sigma\,\mathcal{N}^{-1/3}$, where σ is the standard deviation of the data and $\mathcal{N}$ is the number of data points. Boxplots in the presented figures show the $25\% - 75\%$ range of the distributions around the indicated medians. The significance of having two different distributions is quantified with a rank sum test.

To assess the traction dynamics quantitatively, we first employ a correlation measure R_τ based on the definition

$$
\begin{aligned}
R'_\tau &\equiv \langle \tilde{\mathbf{t}}_{m,n} \cdot \tilde{\mathbf{t}}_{m,n+\tau/\Delta} \rangle_{m,n} \\
&= \frac{2}{N\,M} \sum_{n=1}^{N/2} \sum_{m=1}^{M} \left[\tilde{t}_{x,m,n} \tilde{t}_{x,m,n+\tau/\Delta} + \tilde{t}_{y,m,n} \tilde{t}_{y,m,n+\tau/\Delta} \right].
\end{aligned}
\tag{2}
$$

Here, $\tilde{\mathbf{t}}_{m,n} = \{\tilde{t}_{x,m,n}, \tilde{t}_{y,m,n}\}$ is the traction vector at position $m \in [1, \ldots, M]$ in the movie frame $n \in [1, \ldots, N]$. Δ denotes the time between each frame. The lag time τ of the correlation is in the range $[0, \Delta N/2]$. The traction correlations are measured in the vicinity of the cells. As a reference, we also record correlations of traction far away from cells. Then, correlations of real traction and noise are both normalized by the zero-lag correlation of real traction $R'_0|_{\mathrm{cells}}$ as $R_\tau \equiv R'_\tau / R'_0|_{\mathrm{cells}}$. As shown in Fig. S13, the constant, non-zero value for long times is a result of the finite prestress.

To obtain an alternative measure of traction correlations, one first subtracts the temporal mean of the traction as $\hat{\mathbf{t}}_{m,n} = \tilde{\mathbf{t}}_{m,n} - \langle \tilde{\mathbf{t}}_{m,n} \rangle_n$ and then calculates

$$
r'_\tau = \langle \hat{\mathbf{t}}_{m,n} \cdot \hat{\mathbf{t}}_{m,n+\tau/\Delta} \rangle_{m,n}.
\tag{3}
$$

We normalize again with the zero-lag correlation $r_\tau = r'_\tau / r'_{\tau=0}$. The correlation measure r_τ is similar to R_τ, but decays for large τ to a smaller constant than R_τ since the effect of prestress in the gel is largely removed. Results involving the correlation measure r_τ can be found in in Fig. S8 below.

Velocity autocorrelations in frame n of the movie are calculated from the cell velocities $\mathbf{v}_k(t) = \mathbf{v}_k(n\Delta) = \{v_{x,k,n}, v_{y,k,n}\}$ where k is a unique index for every bacterium. For a fixed time lag τ, the correlation results from averaging over all bacteria $k \in [1, \ldots, K]$ and over time frames n as

$$C'_\tau \equiv \langle \mathbf{v}_{k,(n+\tau/\Delta)} \cdot \mathbf{v}_{k,n} \rangle_{k,n} =$$
$$\frac{2}{N K} \sum_{n=1}^{N/2} \sum_{k=1}^{K} \left[v_{x,k,n} v_{x,k,(n+\tau/\Delta)} + v_{y,k,n} v_{y,k,(n+\tau/\Delta)} \right]. \tag{4}$$

The normalized autocorrelation is then calulated as $C_\tau = C'_\tau / C'_0$. As a measure for the timescale of reorientation we average the cosines of the angles between velocities at different time lags as $A_\tau \equiv \langle \frac{\mathbf{v}_{k,(n+\tau/\Delta)}}{\|\mathbf{v}_{k,(n+\tau/\Delta)}\|} \cdot \frac{\mathbf{v}_{k,n}}{\|\mathbf{v}_{k,n}\|} \rangle_{k,n}$.

References

1. Sun M, Wartel M, Cascales E, Shaevitz JW, Mignot T (2011) Motor-driven intracellular transport powers bacterial gliding motility. *Proc. Nat. Acad. Sci.* 108(18):7559.
2. Luciano J, et al. (2011) Emergence and modular evolution of a novel motility machinery in bacteria. *PLoS Genet.* 7(9):e1002268.
3. Faure LM, et al. (2016) The mechanism of force transmission at bacterial focal adhesion complexes. *Nature* 539(7630):530.
4. Sabass B, Gardel ML, Waterman CM, Schwarz US (2008) High resolution traction force microscopy based on experimental and computational advances. *Biophys. J.* 94(1):207.
5. Flanagan LA, Ju YE, Marg B, Osterfield M, Janmey PA (2002) Neurite branching on deformable substrates. *Neurorept.* 13(18):2411.
6. Ducret A, Valignat MP, Mouhamar F, Mignot T, Theodoly O (2012) Wet-surface–enhanced ellipsometric contrast microscopy identifies slime as a major adhesion factor during bacterial surface motility. *Proc. Nat. Acad. Sci.* 109(25):10036.
7. Plotnikov SV, Sabass B, Schwarz US, Waterman CM (2014) High-resolution traction force microscopy. *Methods Cell Biol.* 123:367.
8. Landau LD, Lifshitz EM (1986) *Course of theoretical physics, Theory of elasticity*. (Pergamon Press Oxford).
9. Schwarz US, et al. (2002) Calculation of forces at focal adhesions from elastic substrate data: the effect of localized force and the need for regularization. *Biophys. J.* 83(3):1380.
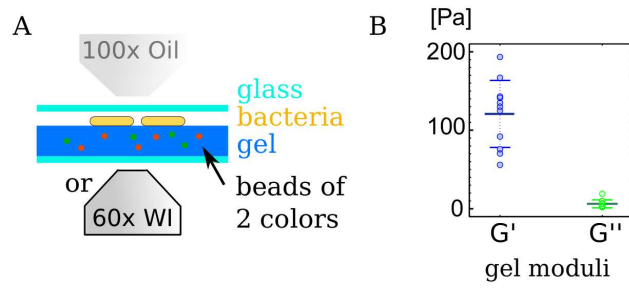
Fig. S1. Setup for traction force microscopy. A) Sketch of the setup for traction force microscopy. Cells are placed on a gel containing fluorescent marker beads of two colors. Individual bacteria are imaged from above with a $100\times$ objective. For bacterial groups, a $60\times$ water immersion objective (WI) is used occasionally. B) The substrates employed for the experiments are polyacrylamide (PAA) gels with storage modulus G' and loss modulus G". Mean $\pm$ standard deviation are plotted over measured data.
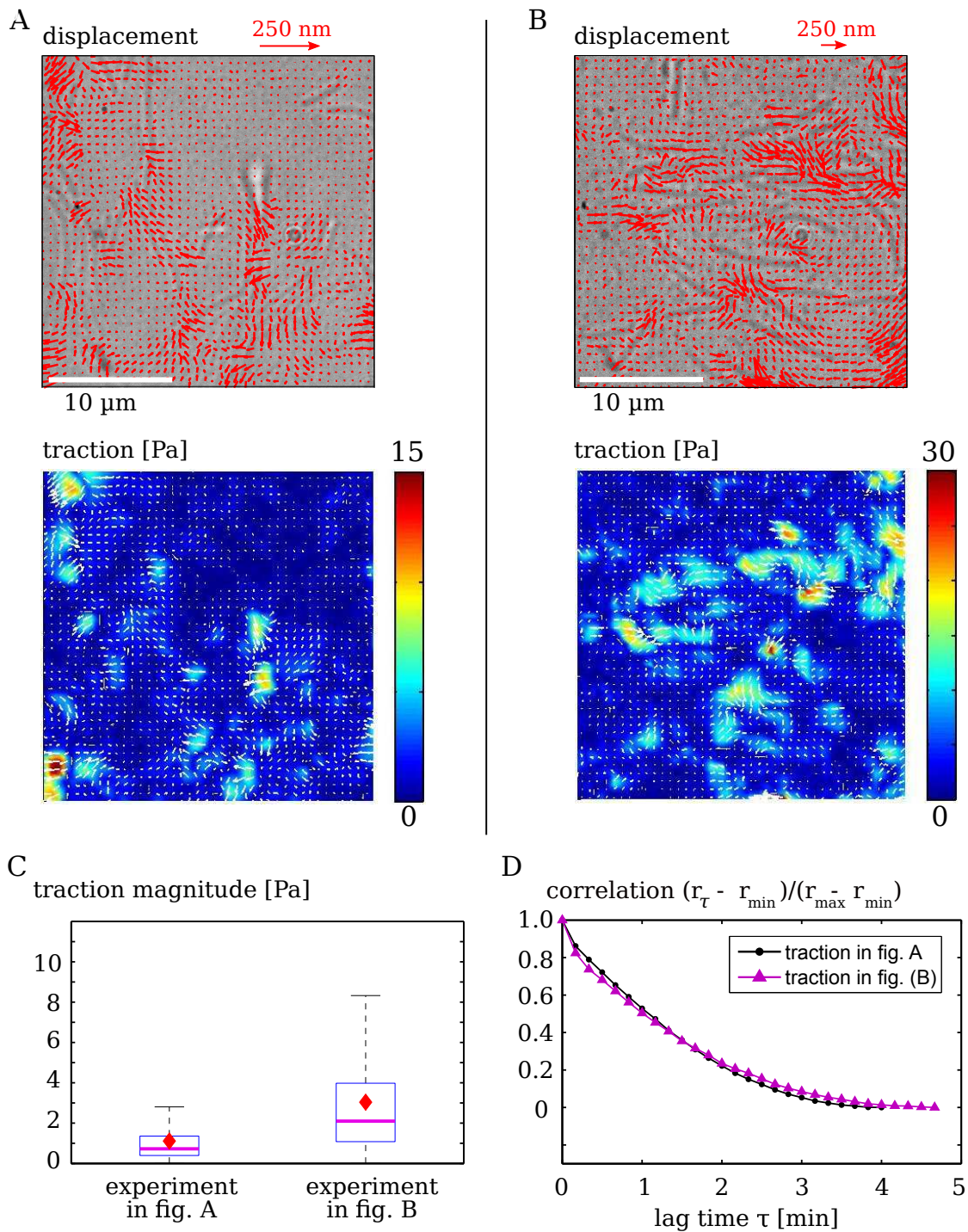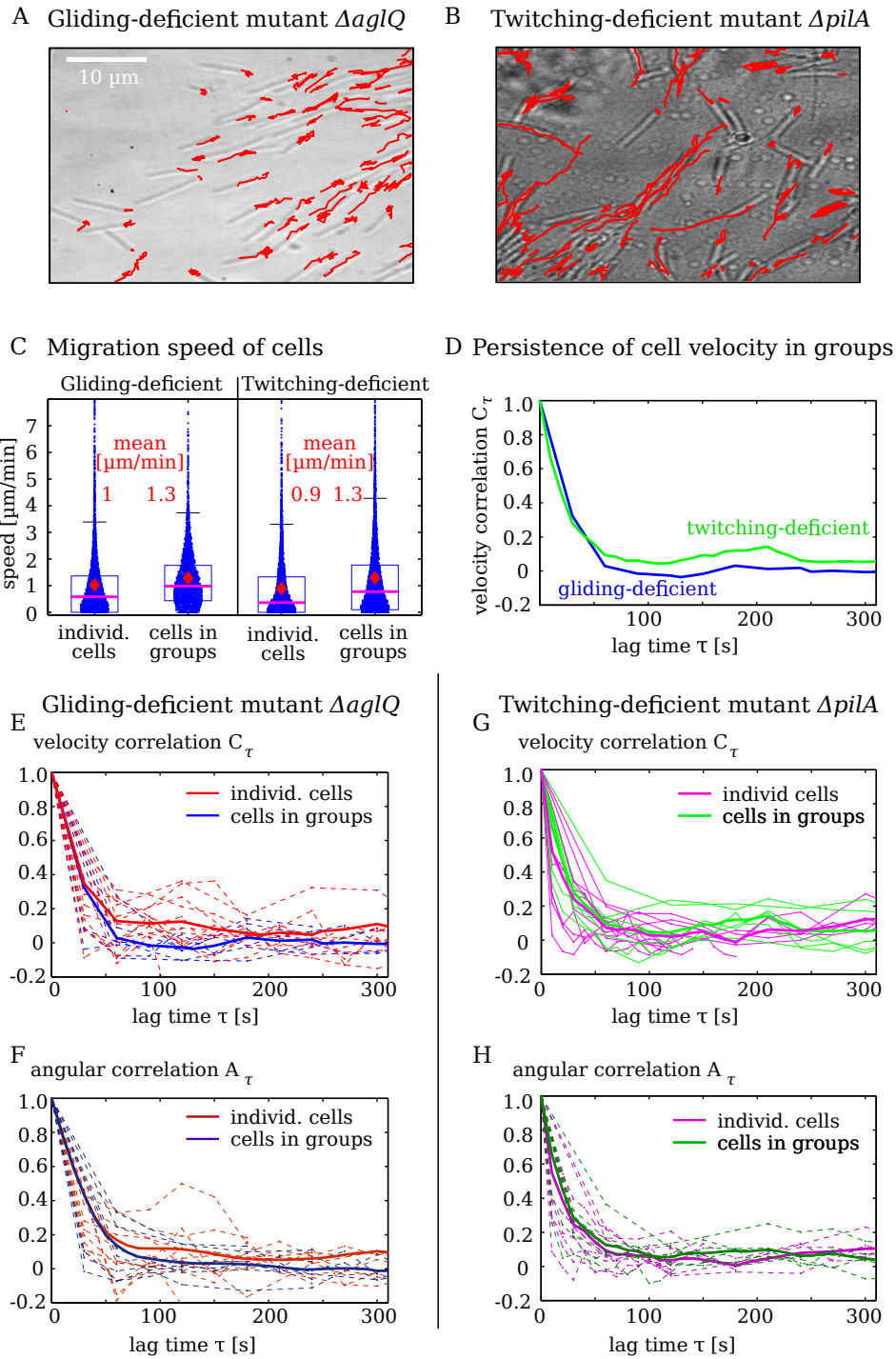
Fig. S2. Two experiments using the wild-type strain DZ2 that can twitch and glide. A) Snapshot showing gel displacements and traction of an experiment with few traction hotspots, suggesting that only very few pili are active. B) Snapshot showing gel displacements and traction of an experiment with many traction hotspots. C) Traction magnitude around cells is stronger in experiment shown in B). D) Traction correlations in both experiments decay within minutes (sampling rate $10s$). The correlation measure r is defined as the measure R in the main text, however, traction at every spatial position is subtracted by its temporal average. For better visibility, only every 3rd quiver is shown.
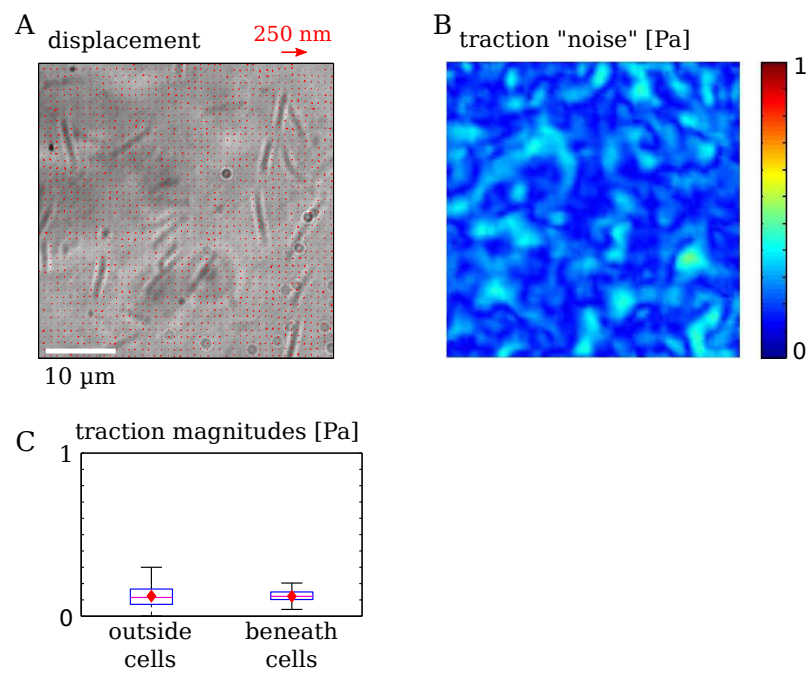
Fig. S3. Control experiment demonstrating absence of traction for a double mutant that can neither twitch nor glide $\Delta aglQ + \Delta PilA$. A) The double mutants produce no significant gel displacement. B) Measurement error results in low traction noise that is randomly distributed. C) Traction noise beneath cells and outside cells is similar.

A Gliding-deficient mutant *ΔaglQ*

B Twitching-deficient mutant *ΔpilA*

C Migration speed of cells

D Persistence of cell velocity in groups

E Gliding-deficient mutant *ΔaglQ*
velocity correlation C_τ

G Twitching-deficient mutant *ΔpilA*
velocity correlation C_τ

F angular correlation A_τ

H angular correlation A_τ

Fig. S4. Characterization of bacterial motion on chitosan-coated substrates. A),B) Trajectories of cells recorded over 13.5 minutes with a time interval of 30s. C) mean instantaneous speed of bacteria is on the order of 1 $\mu m/s$, where bacteria in groups are significantly faster. Boxes contain 75% of data. Violet line is the median. D) Velocity autocorrelation of bacteria in groups C_τ, averaged over multiple experiments. Twitching-deficient $\Delta pilA$ cells have a non-vanishing autocorrelation for long times, indicating a slightly persistent motion. Twitching-deficient $\Delta aglQ$ mutants in groups exhibit rapidly decorrelated motion. E)-F) Velocity correlations C_τ and correlation of the direction of motion A_τ for $\Delta aglQ$ mutants. Thin lines are average values from one experiment, thick lines are averages over all experiments. Correlations decay within 1 min. For cells in groups, correlations vanish almost completely while individually migrating cells maintain a weakly correlated velocity. G)-H) E)-F) Velocity correlations C_τ and correlation of the direction of motion A_τ for ΔpiA. Data for C)-H) results from 7 separate experiments for groups of each kind and 13 experiments for single cells of each kind. Each experiment contains between 10 and 60 cells. Images captured at time intervals of $[10-60]$ s.
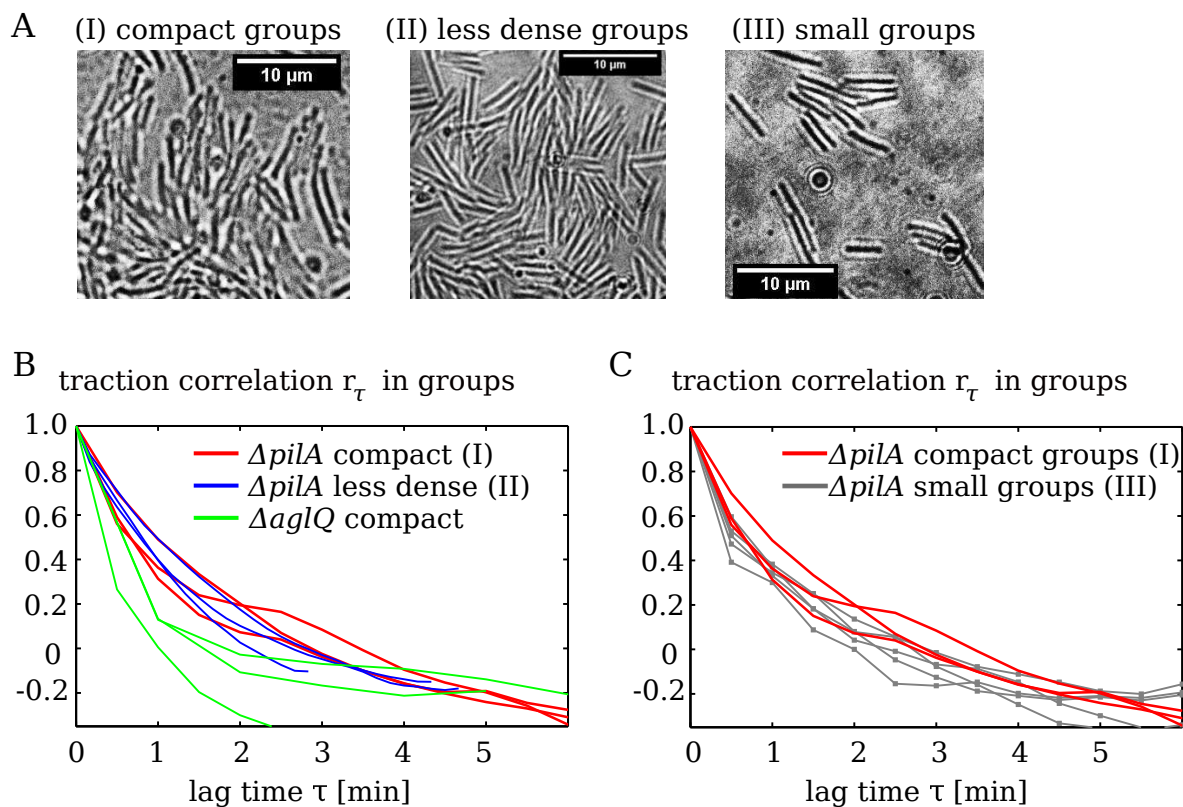
A   Migration of individual cells

B   Migration of cells in groups
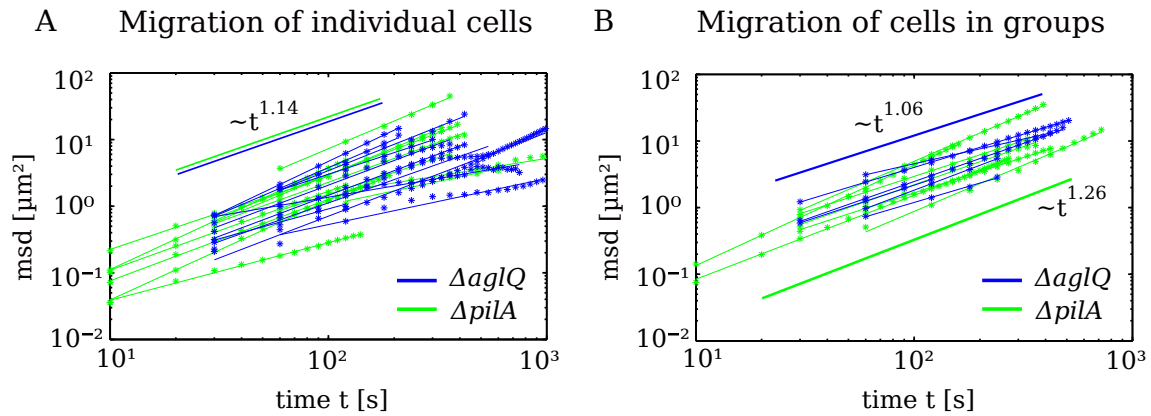
Fig. S5. Mean squared displacement of bacteria is defined as $\mathrm{msd}(t) \equiv <|\mathbf{r}_\mathrm{n}(t_0 + t) - \mathbf{r}_\mathrm{n}(t_0)|^2 >_{t_0, n}$ where n is the index labeling bacteria. Asterisks are average msd in one experiment, where each experiment contains between 10 and 50 cells. Data for each experiment are fitted to a power law $msd(t) \sim t^\alpha$. Thick lines show the average of α. Normal random diffusion is characterized by $\alpha = 1$. A) Msd of cells that move individually outside of groups. The average exponents are $\alpha_{pilA} \simeq 1.14$ (std: 0.3), $\alpha_{aglQ} \simeq 1.14$ (std: 0.28). B) Msd of cells moving inside groups. Average average exponents are $\alpha_{pilA} \simeq 1.26$ (std: 0.18), $\alpha_{aglQ} \simeq 1.06$ (std: 0.18). For groups, the data indicates that twitching-deficient $\triangle pilA$ mutants undergo superdiffusive motion while the motion of gliding-deficient $\triangle aglQ$ mutants is more similar to normal diffusion.
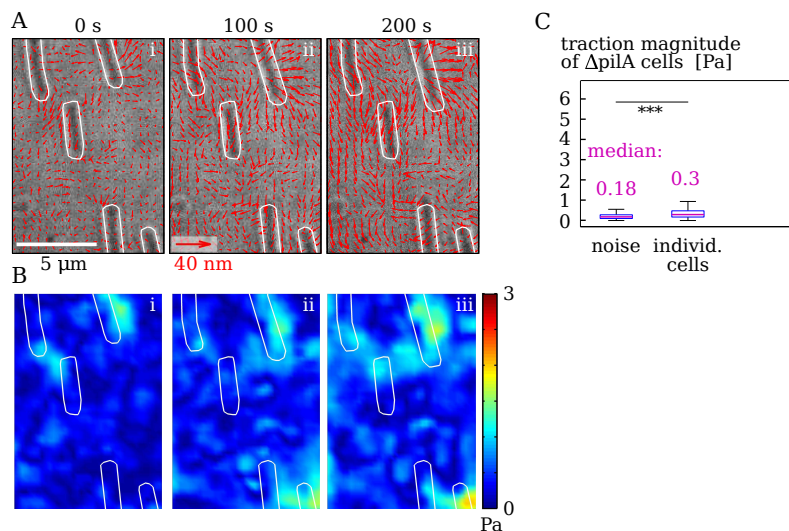

Fig. S6. Traction during gliding of individual bacteria from a strain without pili ($\triangle PilA$). A) Quiver plots of gel displacement. B) Calculated traction. The gel displacements beneath individual gliding bacteria are very small, $< 20\,\mathrm{nm}$, and can hardly be distinguished from detection noise. As a result, traction estimation is error-prone. C) Box plots showing the distribution of traction noise measured outside of cells and traction measured immediately beneath cells.
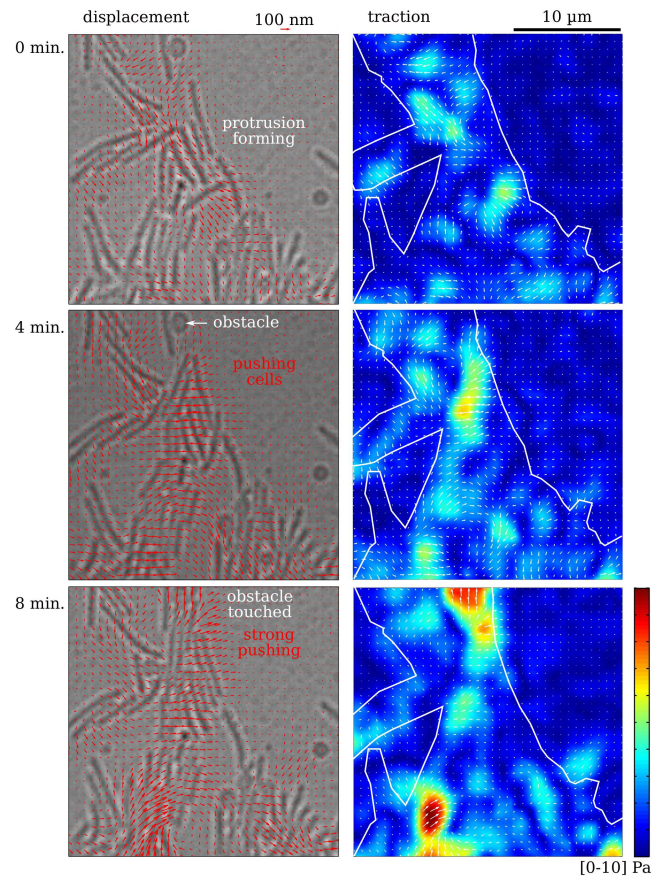
Fig. S7. Gliding cell groups can form protrusions where cells collectively push in the direction of migration. At 8 minutes, pushing is amplified by contact with an obstacle. For better visibility, only every second vector is shown.

Sabass *et al.*

A (I) compact groups (II) less dense groups (III) small groups

B traction correlation r_τ in groups

- $\Delta pilA$ compact (I)
- $\Delta pilA$ less dense (II)
- $\Delta aglQ$ compact

lag time τ [min]

C traction correlation r_τ in groups

- $\Delta pilA$ compact groups (I)
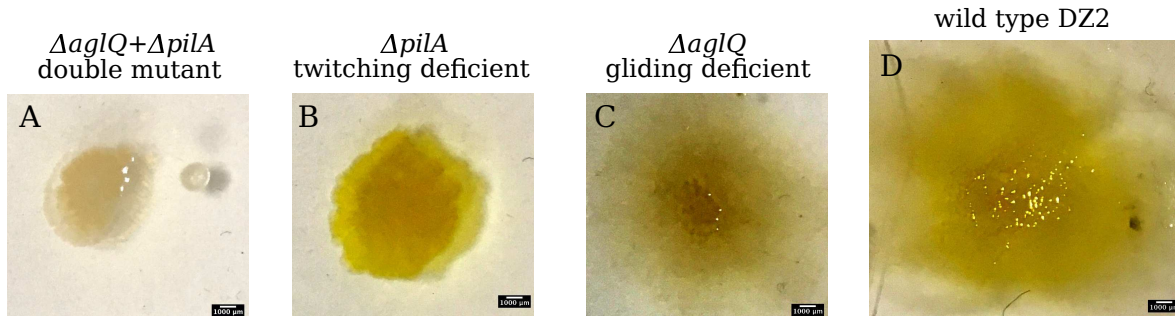- $\Delta pilA$ small groups (III)

lag time τ [min]

Fig. S8. Dependence of traction correlation on the structure and size of groups of gliding $\Delta pilA$ mutants. A) Snapshots illustrating the three conditions that are compared:(I) compact groups, (II) less dense groups, (III) small groups containing only a few cells. B) Traction correlation is similar for compact and less dense groups. Each line represents data from one experiment. For comparison, correlations from three groups of twitching $\Delta pilA$ mutants is shown C) Traction correlation in small groups does not show pronounced differences to traction correlations in compact groups.
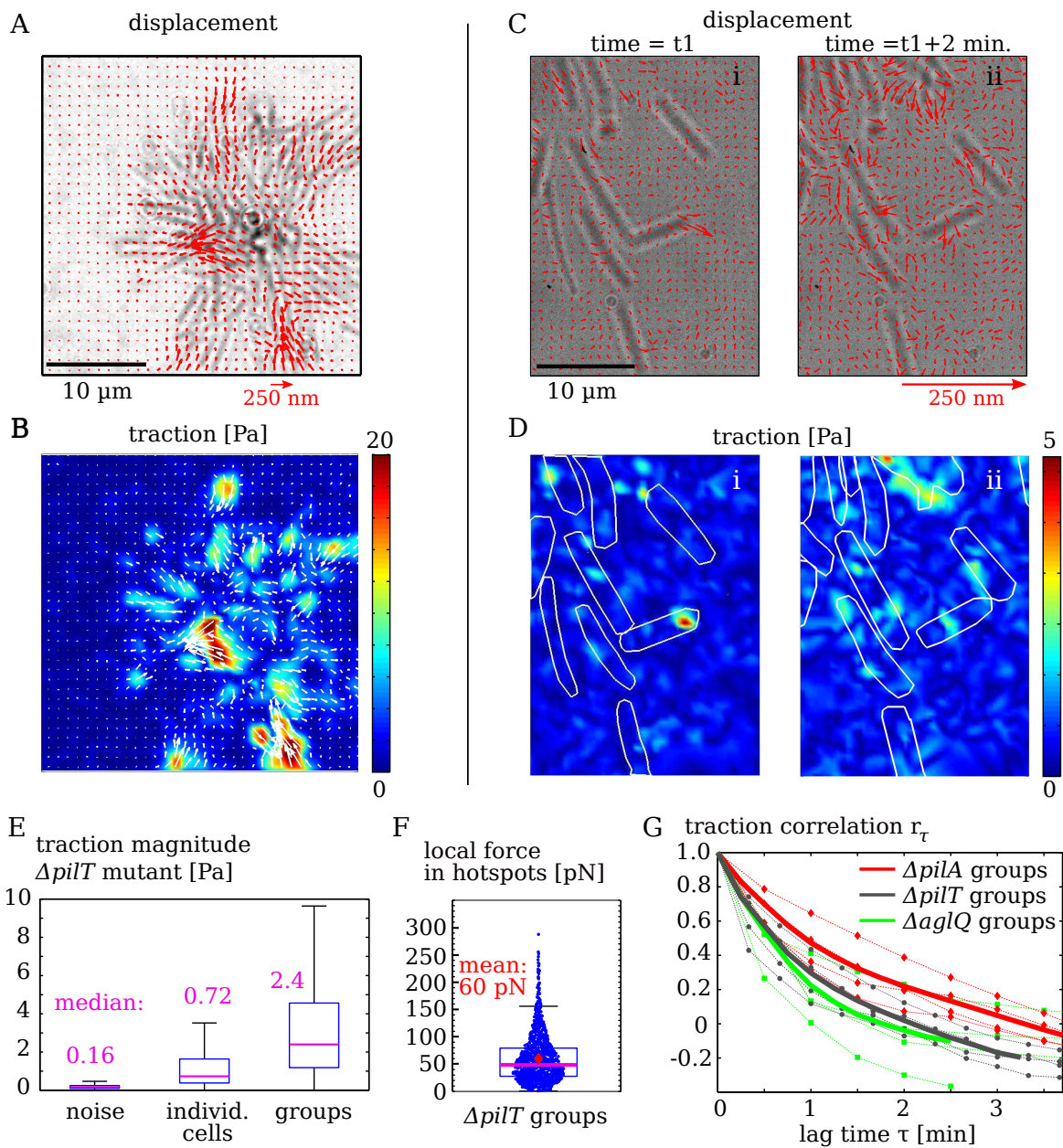
Fig. S9. Experiments using a $pilT$ mutant with impaired pilus retraction machinery. A) Snapshot showing gel displacement. B) Snapshot showing traction of the same colony above. C) Gel displacement under individual cells is small. D) Traction under individual cells is small and almost on comparable to the noise background. E) Traction magnitude distributions. Noise is measured away from cells, traction below individual cells and groups is measured only directly under cells. F) Force magnitude of hotspots under groups. Dots are individual measurements and violet bar is the median. The mean force of $60\,\mathrm{pN}$ is smaller than the mean of $\sim 100\,\mathrm{pN}$ observed for the $\triangle aglQ$ with unimpaired pilus retraction machinery. G) Traction correlation of $\triangle pilT$, $\triangle pilA$, and $\triangle aglQ$ mutants. Thick lines are averages over four experiments. The correlation decay varies considerably between experiments, but indicates that groups of $\triangle pilT$ exhibit faster traction dynamics than gliding $\triangle pilA$ cells. Such dynamics could possibly result from some sort of pilus retraction or extension that is independent of $pilT$ and occurs in groups of $\triangle pilT$ mutants. Data for cell groups in E),F) collected from 3 separate movies. Data for individual cells collected from 35 cells in 6 separate movies. Correlation data in G) collected from 4 movies with each mutant.

ΔaglQ+ΔpilA
double mutant

ΔpilA
twitching deficient

ΔaglQ
gliding deficient

wild type DZ2

Fig. S10. Spreading and growth of bacterial colonies on chitosan-coated PAA in growth medium. Snapshots were taken after 48h of incubation. Before plating, cells were grown in an overnight culture and then washed with tpm. $10\ \mu$l of bacterial suspension with an optical density of 0.8 were spotted on to the substrate. Bars: $1\ \mathrm{mm}$

ΔpilA
twitching deficient

ΔaglQ
gliding deficient
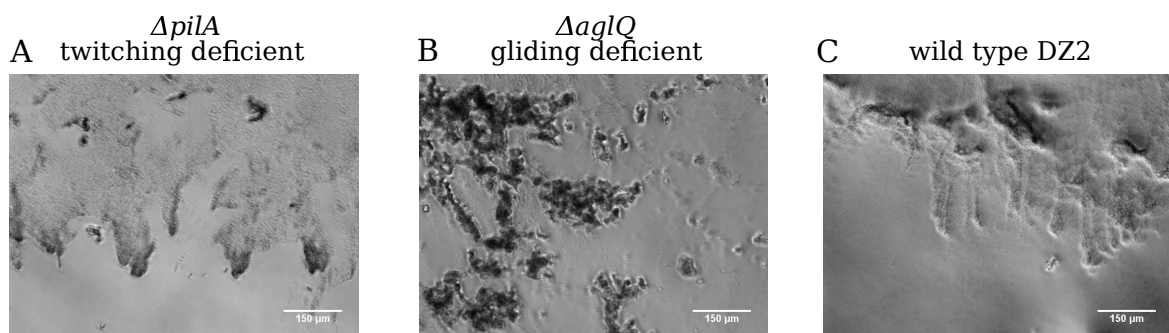
wild type DZ2

Fig. S11. Spreading due to migration of bacterial colonies on chitosan-coated PAA in nutrient-poor medium TPM. Images were taken 20 min. after the cultures were washed and $10\ \mu$l were spotted on the plates. While wild-type and gliding $\Delta pilA$ strains clearly form protruding colony edges, the $\Delta aglQ$ strain produces cell clumps at the edges with only few cells migrating outward at this stage. Bars: $0.15\ \mathrm{mm}$
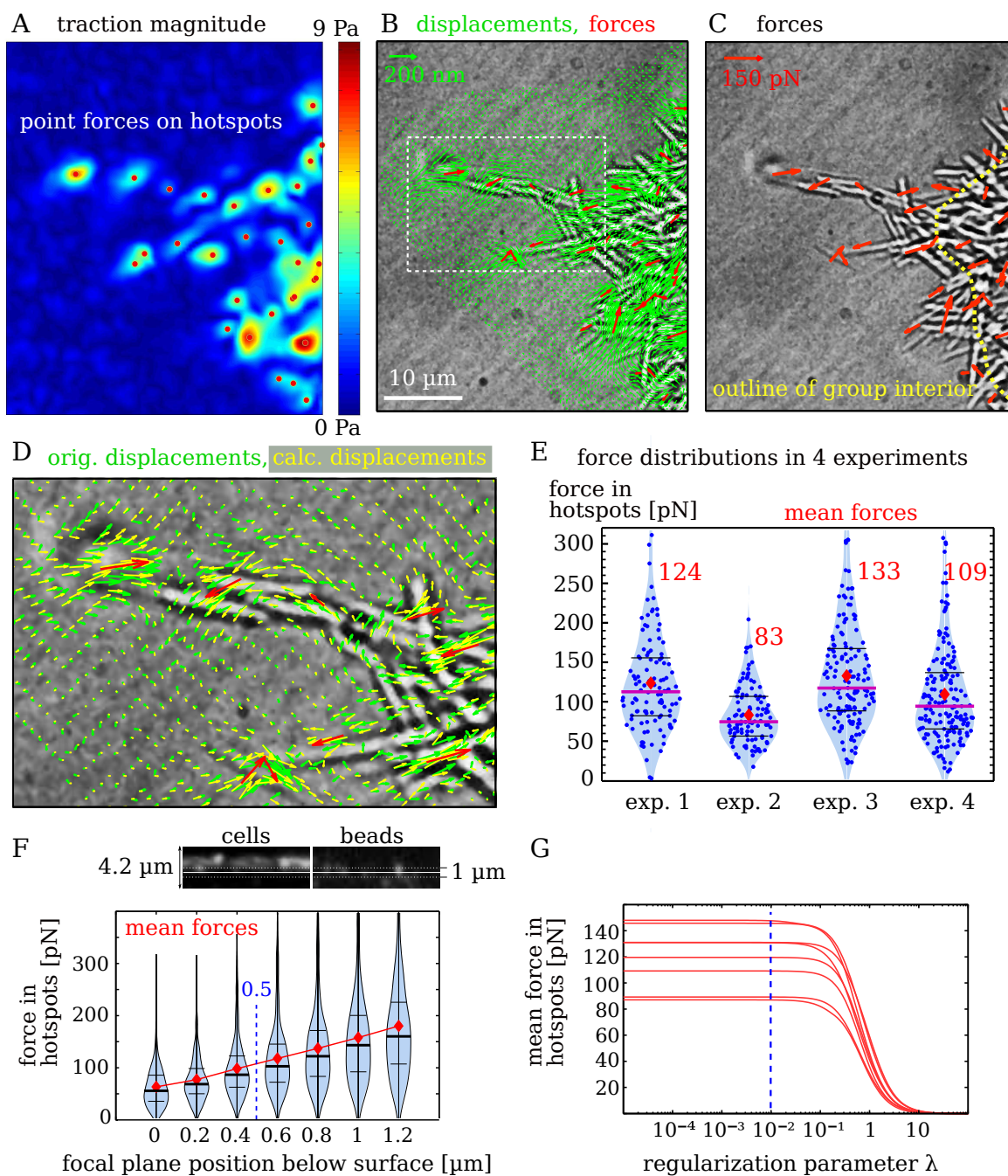
Fig. S12. Estimation of force magnitude in traction hotspots created by pili. A) Reconstructed traction field contains hotspots. Using these traction maps, a point is placed inside each hotspot. B) Assuming that all force is concentrated at these points, we perform a maximum likelihood estimate of forces from the measured displacements. C) Point forces form rather disorganized patterns with opposing forces being close to each other. D) Magnified displacement data from the region of interest indicated in (B). Green quivers show original displacements, yellow quivers show the displacements that were back-calculated from the inferred point-forces. For clearer visibility, only every second quiver is shown. E) Comparison of force magnitudes measured in 4 separate experiments with each 4 images. Data in (A-D) is from experiment 2. F) Dependence of force on vertical position of the imaging plane below the gel surface. Due to the finite point spread function, beads lie slightly below the surface of the gel. Images show side-view of cells with beads and the position of the focal plane. The force magnitude increases with the assumed vertical distance between the gel surface and the plane in which displacements are measured. A distance of $0.5\ \mu m$ is consistent with the vertical image scans and was therefore used for the analysis. F) Dependence of average point forces on the regularization parameter λ for different experiments. λ is given in units of $1/\text{pix}$ since displacements are measured in pixels and forces are scaled by $\text{Pa}\,\mu m^2/\text{pix}^2$. We employ $\lambda = 0.01$ to regularize force magnitude as little as possible and consistently for all data sets.
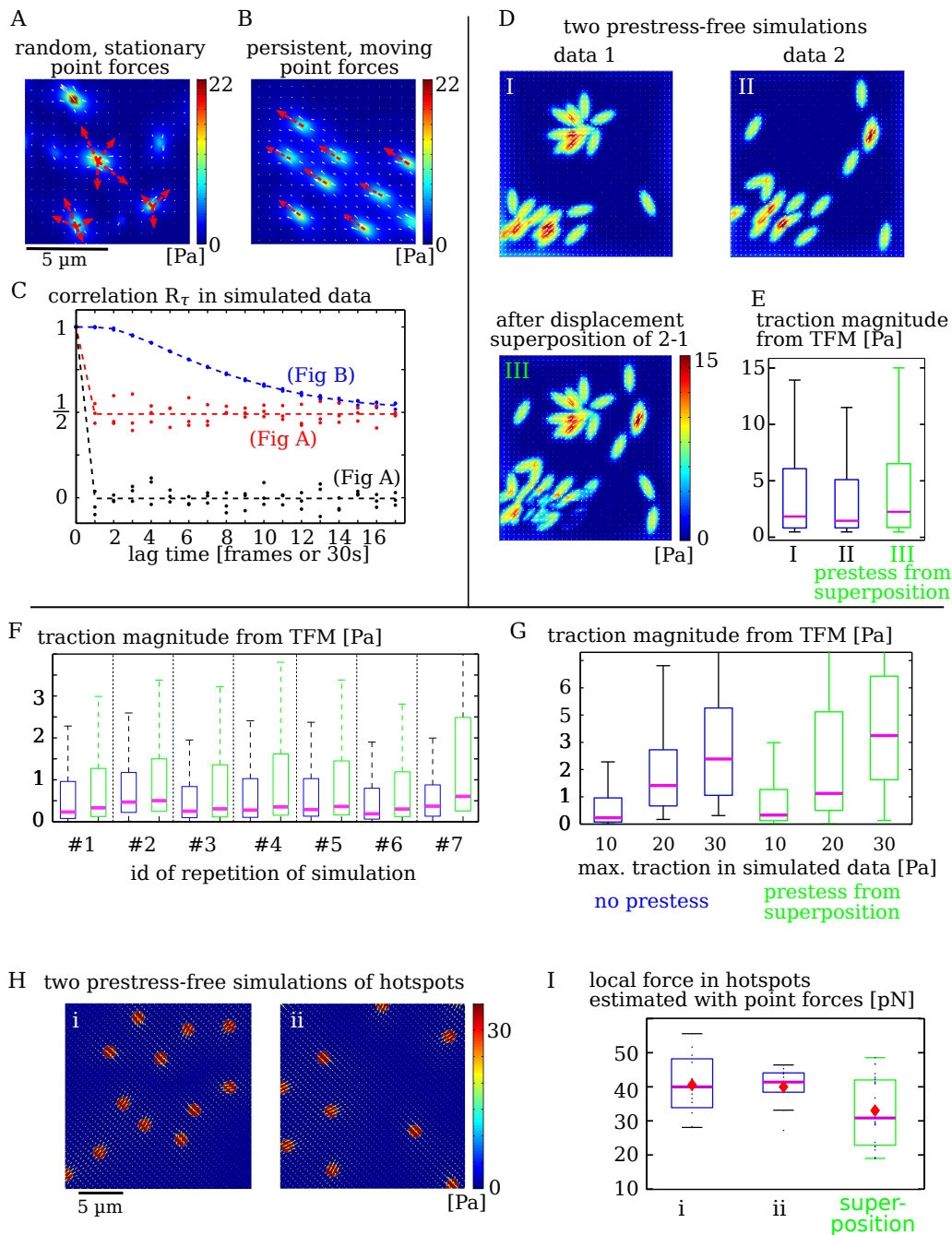
Fig. S13. Simulation of artificial data to test the TFM results. A) Simulation of random stationary point forces. Forces are chosen in each frame from a Gaussian distribution. The resulting gel deformation is calculated for a vertical bead depth of $0.5\ \mu m$ with a pixel size of $0.0607\ \mu m$. Subsequently, the resulting displacement field is used as input for the calculation of traction and the correlation mesure R_τ. B) Simulation of moving point forces of constant magnitude. Points move in the direction of force with a constant speed of $0.5\ \mu m/s$. C) Correlation R_τ of reconstructed traction forces in simulations. Black dots: Simulation of stationary, random forces as shown in A). Gel displacements are calculated with respect to a stress-free reference state. As expected, we find $R_\tau \simeq 0$ for $\tau > 0$. Red data: Simulation of stationary, random forces as shown in A), but displacements are now calculated with respect to the first frames of the movies. The prestress in the reference state leads to constant $R_\tau \simeq 0.5$ for finite time lag. Blue data: Simulations of persistently moving point forces as shown in B) where displacements are calculated with respect to the first frames of the movies. Motion of the forces leads to a slow decay of correlation towards $R_\tau \simeq 0.5$ for large lags. For each condition, the data was generated from three simulations of each 35 frames.

D) Simulation of two traction patterns (I-II) where ellipsoidal regions are submitted to locally constant traction. (III) Illustration of the effect of strong prestress where displacements calculated in (I) are subtracted from the displacements in (II). Note that prestress affects traction strongest if the traction regions overlap. E) Traction magnitudes resulting from applying TFM to the simulations illustrated in D(I-III). Prestress can increase or decrease traction magnitude. Violet line is median. E) Reconstructed traction with and without prestress in 7 simulations using different locations of traction spots as shown in (D). Violet line is median. Prestress affects spread of data and median, but still allows to distinguish relative differences approximately. F) Reconstructed traction with and without prestress in simulations with different traction magnitude. Prestress does not prohibit to distinguish relative traction magnitude levels.

H) Two simulation (i-ii) of small circular traction regions to imitate hotspots. I) Overall force magnitude of every hotspots estimated using point forces. To assess the role of prestress, original prestress-free forces (i-ii) are compared with a data set where the displacements calculated in the two simulations are subtracted from each other. In this example, prestress leads to an error of $\sim 25\,\%$ in the mean.